


 Cite this: *RSC Adv.*, 2022, 12, 2462

# Synthesis and characterisation of heteroatom-doped reduced graphene oxide/bismuth oxide nanocomposites and their application as photoanodes in DSSCs†

 Nonjabulo P. D. Ngidi,  Edigar Muchuweni  ‡ and Vincent O. Nyamori  \*

Semiconductor materials have been recently employed in photovoltaic devices, particularly dye-sensitized solar cells (DSSCs), to solve numerous global issues, especially the current energy crisis emanating from the depletion and hazardous nature of conventional energy sources, such as fossil fuels and nuclear energy. However, progress for the past years has been mainly limited by poor electron injection and charge carrier recombination experienced by DSSCs at the photoanode. Thus, novel semiconductor materials such as bismuth oxide ( $\text{Bi}_2\text{O}_3$ ) have been investigated as an alternative photoanode material. In this study,  $\text{Bi}_2\text{O}_3$  was integrated with nitrogen- or boron-doped reduced graphene oxide (N-rGO or B-rGO, respectively) via a hydrothermal approach at a temperature of 200 °C. Various instrumental techniques were used to investigate the morphology, phase structure, thermal stability, and surface area of the resulting nanocomposites. The incorporation of N-rGO or B-rGO into  $\text{Bi}_2\text{O}_3$  influenced the morphology and structure of the nanocomposite, thereby affecting the conductivity and electrochemical properties of the nanocomposite. B-rGO/ $\text{Bi}_2\text{O}_3$  exhibited a relatively large surface area ( $65.5 \text{ m}^2 \text{ g}^{-1}$ ), lower charge transfer resistance ( $108.4 \ \Omega$ ), higher charge carrier mobility ( $0.368 \text{ cm}^2 \text{ V}^{-1} \text{ s}^{-1}$ ), and higher electrical conductivity ( $6.31 \text{ S cm}^{-1}$ ) than N-rGO/ $\text{Bi}_2\text{O}_3$ . This led to the fabrication of B-rGO/ $\text{Bi}_2\text{O}_3$  photoanode-based DSSCs with superior photovoltaic performance, as revealed by their relatively high power conversion efficiency (PCE) of 2.97%, which outperformed the devices based on N-rGO/ $\text{Bi}_2\text{O}_3$ , rGO/ $\text{Bi}_2\text{O}_3$ , and  $\text{Bi}_2\text{O}_3$  photoanodes. Therefore, these results demonstrate the promising potential of heteroatom-doped rGO/ $\text{Bi}_2\text{O}_3$ -based nanocomposites as photoanode materials of choice for future DSSCs.

 Received 7th December 2021  
 Accepted 11th January 2022

DOI: 10.1039/d1ra08888b

[rsc.li/rsc-advances](https://rsc.li/rsc-advances)

## 1 Introduction

Recent developments in technology have led to a tremendous demand for energy. Thus, renewable energy sources, especially solar energy, which can be converted to electrical energy by photovoltaic devices, particularly dye-sensitized solar cells (DSSCs), have been favoured by many researchers.<sup>1–5</sup> The main component of DSSCs is the photoanode, which is responsible for transferring photogenerated electrons from the excited dye molecules to the collecting electrode. Thus, a high electron-transport rate reduces the charge recombination rate and improves the power conversion efficiency (PCE). The

development of DSSCs by means of tailoring the properties of semiconductor nanomaterials to suit photoanode applications has attracted a lot of attention in solar energy research. This is because semiconductor nanomaterials have unique physical, chemical, electronic and optical properties. Semiconductor photoanode nanomaterials with a high surface area can facilitate more dye absorption, effective photon harvesting, and fast charge transport, thereby improving the PCE of DSSCs. Various approaches, such as doping,<sup>6</sup> surface modification,<sup>7</sup> and the use of hybrid semiconducting nanomaterials,<sup>8–12</sup> have been proposed to improve the properties of semiconductor materials. Semiconductor nanomaterials such as metal oxides, including titanium dioxide ( $\text{TiO}_2$ ),<sup>13</sup> zinc oxide ( $\text{ZnO}$ ),<sup>14</sup> zirconium dioxide ( $\text{ZrO}_2$ ),<sup>15</sup> tungsten trioxide ( $\text{WO}_3$ ),<sup>16</sup> and tin(IV) oxide ( $\text{SnO}_2$ ),<sup>17</sup> have been extensively explored as photoanode materials in DSSCs.

To date, there are few studies based on the application of bismuth oxide ( $\text{Bi}_2\text{O}_3$ ) as a photoanode in DSSCs, yet  $\text{Bi}_2\text{O}_3$  has attracted great interest in photocatalysis<sup>18</sup> and supercapacitors<sup>19</sup> due to its unique crystal structure,<sup>20</sup> non-toxicity,<sup>21</sup> and wide

School of Chemistry and Physics, University of KwaZulu-Natal, Westville Campus, Private Bag X54001, Durban, 4000, South Africa. E-mail: [nyamori@ukzn.ac.za](mailto:nyamori@ukzn.ac.za); [nonjabulongidi@gmail.com](mailto:nonjabulongidi@gmail.com); [muchuwenie@ukzn.ac.za](mailto:muchuwenie@ukzn.ac.za); Fax: +27-31-2603091; Tel: +27-31-2608256

† Electronic supplementary information (ESI) available. See DOI: 10.1039/d1ra08888b

‡ On leave from Bindura University of Science Education, Department of Engineering and Physics, Private Bag 1020, Bindura, Zimbabwe.



bandgap, ranging from 2.47 to 3.55 eV.<sup>22</sup> Bi<sub>2</sub>O<sub>3</sub> also exhibits a high dielectric permittivity, refractive index, photoconductivity, and oxygen ion conductivity. There are four polymorphs of Bi<sub>2</sub>O<sub>3</sub>, namely, body-centred cubic ( $\gamma$ ), face-centred cubic ( $\delta$ ), tetragonal ( $\beta$ ) and monoclinic ( $\alpha$ ).<sup>23</sup> Among these,  $\alpha$ -Bi<sub>2</sub>O<sub>3</sub> and  $\delta$ -Bi<sub>2</sub>O<sub>3</sub> are thermodynamically stable at ambient conditions, whereas  $\beta$ -Bi<sub>2</sub>O<sub>3</sub> and  $\gamma$ -Bi<sub>2</sub>O<sub>3</sub> are metastable, and are stabilised by the addition of impurities or by controlling the reaction conditions.<sup>24</sup> An investigation on the effect of  $\beta$ -Bi<sub>2</sub>O<sub>3</sub> as a photoanode in DSSCs has been reported by Shaikh *et al.*<sup>25</sup> and resulted in a PCE of 0.078%. However, a slight improvement in the PCE to 1.5% was observed when  $\beta$ -Bi<sub>2</sub>O<sub>3</sub> was incorporated with ZnO. Fatima *et al.*<sup>26</sup> reported a PCE of 0.05% for DSSCs with  $\alpha$ -Bi<sub>2</sub>O<sub>3</sub>-based photoanodes. The low PCE was attributed to the presence of trapping states at the interfaces within the photoanode. Thus, more research on Bi<sub>2</sub>O<sub>3</sub> nanomaterials for photoanode applications in DSSCs is still required.

Recently, metal oxides have been integrated with an allotrope of carbon, especially graphene, and used as positive electrode material in energy storage devices.<sup>27,28</sup> Graphene has attracted significant interest due to its high charge carrier mobility, large specific surface area, high mechanical strength, high electrical conductivity, and chemical resilience. Also, graphene is reported to display predominant energy storage performance compared with other carbon nanostructures, such as carbon nanotubes and graphite.<sup>29,30</sup> Graphene oxide (GO) is defined as a cutting edge of graphene functionalised with carbonyl and carboxyl groups at the edges; and epoxy and hydroxyl groups in the basal plane.<sup>31</sup> The oxygen-based functional groups on the surface of GO are responsible for integrating GO with metal oxides, resulting in GO-based metal oxide nanocomposites.

The main focus in the reported studies of Bi<sub>2</sub>O<sub>3</sub> was to integrate Bi<sub>2</sub>O<sub>3</sub> with reduced graphene oxide (rGO) due to the distinctive mechanical, electrical, and electrochemical properties of rGO.<sup>32–34</sup> This is envisaged to help overcome the drawbacks of pristine rGO, such as its usual tendency to agglomerate or restack to form graphite due to  $\pi$ - $\pi$  stacking and van der Waals forces when the rGO nanosheets are close to each other,<sup>35</sup> resulting in poor electrochemical properties. Nitrogen-doped reduced graphene oxide (N-rGO) and boron-doped reduced graphene oxide (B-rGO) have been reported to have improved electrochemical properties than rGO;<sup>36</sup> thus, integrating Bi<sub>2</sub>O<sub>3</sub> with N-rGO or B-rGO is expected to yield favourable device performance. However, to the best of our knowledge, no detailed studies have reported the electrochemical properties of heteroatom-doped rGO (N-rGO or B-rGO) integrated with Bi<sub>2</sub>O<sub>3</sub> and their application as photoanodes in DSSCs. Hence, in this study, the effect of nitrogen or boron on the physicochemical and electrochemical properties of heteroatom-doped rGO/Bi<sub>2</sub>O<sub>3</sub> nanocomposites was investigated for the first time by means of various instrumental techniques, so as to enhance the electrochemical properties of Bi<sub>2</sub>O<sub>3</sub>, reduce the aggregation of rGO, and subsequently improve the performance of DSSCs.

## 2 Experimental

### 2.1 Materials

Bismuth oxide (Bi<sub>2</sub>O<sub>3</sub>, 99.99%), 4-nitro-*o*-phenylenediamine ( $\geq 99\%$ ), boric anhydride ( $\geq 98\%$ ), boron standard solution (999.5 mg L<sup>-1</sup>  $\pm$  20 mg L<sup>-1</sup>), bismuth standard for ICP trace-Cert® (1000 mg L<sup>-1</sup> Bi in nitric acid), potassium hydroxide (KOH,  $\geq 85\%$ , pellets), Nafion ( $\leq 100\%$ ), lithium iodide (99.9%), 4-*tert*-butylpyridine (98%), guanidinium thiocyanate (99%), 1-methyl-3-propylimidazolium iodide (99.99%), acetonitrile ( $\geq 99.9\%$ ), poly(vinyl acetate) (99.9%), absolute ethanol (99.5%), eosin B (97%) and indium tin oxide (ITO) coated glass slides (15  $\Omega$ , 30  $\times$  30  $\times$  0.7 mm) were purchased from Sigma-Aldrich, South Africa.

### 2.2 Synthesis of the nanocomposite

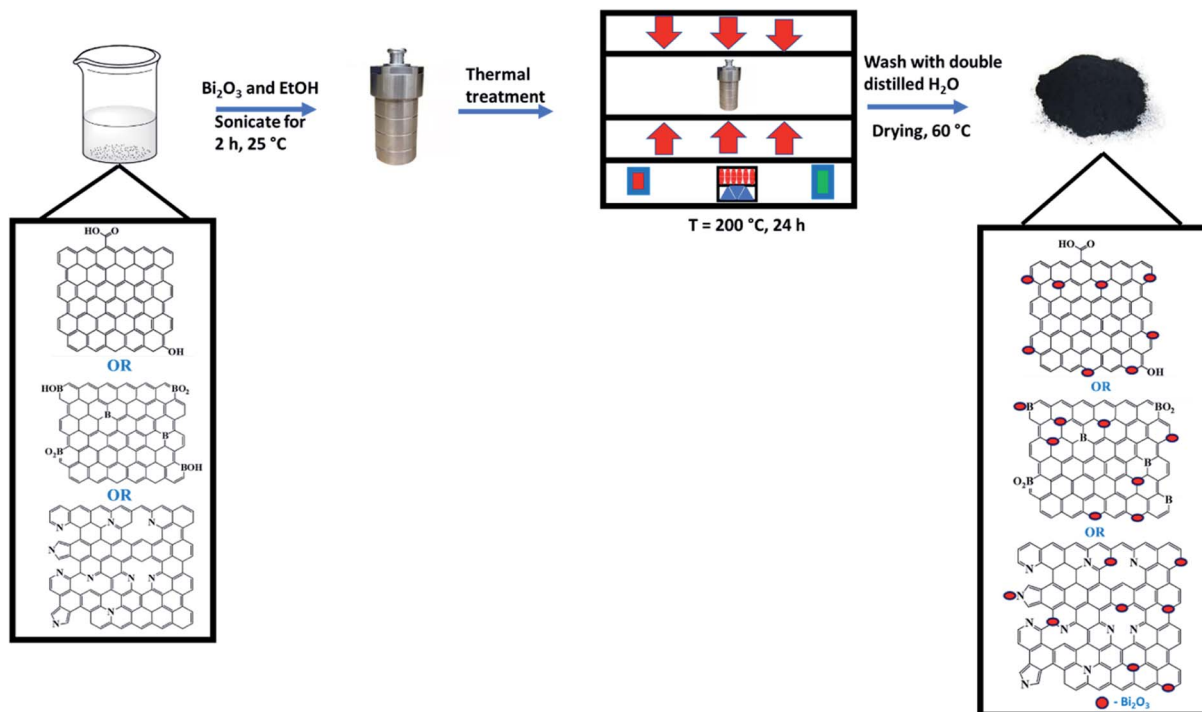
rGO was synthesised *via* thermal annealing of GO at a temperature of 600 °C under 10% H<sub>2</sub> in argon,<sup>37</sup> while N-rGO or B-rGO was synthesised by thermal treatment of GO and a precursor of 4-nitro-*o*-phenylenediamine or boric anhydride, respectively, at a temperature of 600 °C.<sup>38,39</sup> Bi<sub>2</sub>O<sub>3</sub> (0.2 g) and rGO, N-rGO, or B-rGO (0.5 g) were dispersed in absolute ethanol (60 mL) and sonicated for 2 h (Scheme 1). After sonication, the mixtures were transferred into a Teflon-lined stainless-steel autoclave and thermally treated at a temperature of 200 °C for 24 h. The nanocomposites were purified by washing them with double-distilled water, followed by drying the samples in an oven for 24 h at 60 °C before characterisation.

### 2.3 Device fabrication

The Bi<sub>2</sub>O<sub>3</sub>-based nanocomposite (100 mg) was dispersed in absolute ethanol (0.3 mL), sonicated, and deposited onto an ITO glass of the photoanode by using the Doctor Blade method. The photoanode was then annealed at 300 °C for 30 min. After thermal annealing, 0.3 mM eosin B dye (150  $\mu$ L) was loaded onto the photoanode. The iodide/triiodide gel state electrolyte was stained onto the dye-coated photoanode, followed by assembling the aluminium-coated cathode in a sandwich-like fashion. The iodide/triiodide gel state electrolyte was prepared by firstly synthesizing the liquid electrolyte. The liquid electrolyte was synthesised by mixing lithium iodide (0.3348 g), 4-*tert*-butylpyridine (1.6900 g), guanidinium thiocyanate (0.2954 g) and 1-methyl-3-propylimidazolium iodide (0.3173 g) and dissolved in acetonitrile (5 mL). The synthesised liquid electrolyte (1.2484) was mixed with poly(vinyl acetate) (0.6022 g) and stirred using a glass rod until a gel state electrolyte was formed, and further kept in a refrigerator at 0 °C.

### 2.4 Characterisation

Field emission-scanning electron microscopy (FE-SEM, Carl Zeiss Ultra Plus) was used to investigate the surface morphology of the nanocomposites. Transmission electron microscopy (TEM, JEOL JEM, 1010 model) was used to investigate the microstructure of the nanocomposites. The presence of various elements in the nanocomposites was investigated by elemental



Scheme 1 Schematic diagram of the conversion of rGO, N-rGO and B-rGO to  $\text{Bi}_2\text{O}_3$ -based nanocomposites.

analysis (Elementar vario EL cube CHNSO elemental analyser), and  $\text{Bi}_2\text{O}_3$  was quantified *via* inductively coupled plasma-optical emission spectrometry (ICP-OES, PerkinElmer Optima 5300 DV). The presence of various functional groups was determined by Fourier transform infrared spectroscopy (PerkinElmer Spectrum 100, FTIR spectrophotometer, with an attenuated total reflectance (ATR) accessory).

The phase compositions present in the nanocomposites were evaluated by means of powder X-ray diffraction (XRD, Bruker AXS,  $\text{Cu K}_\alpha$  radiation source,  $\lambda = 0.154$  nm). The graphitic nature of the nanocomposites was investigated by a Renishaw inVia Raman microscope at an excitation wavelength of 488 nm. The thermal stability was analysed with a TA Instruments Q series™ thermal analyser DSC/TGA (Q600) instrument. The textural characteristics were determined using a Micromeritics Tristar II 3020 surface area and porosity analyser. The electrical conductivity of the nanocomposites was investigated by a four-point probe (Keithley 2400 source-meter). Hall effect measurements were carried out using an Ecopia Hall effect measurements system, model HMS 3000, equipped with HMS3000 VER 3.15.5 software.

Cyclic voltammetry (CV) and electrochemical impedance spectroscopy (EIS) were carried out on a VersaSTAT3F potentiostat/galvanostat electrochemical workstation, with ZSimpWin software utilised for EIS data analysis. A counter electrode (platinum wire (Pt)), a reference electrode (Ag/AgCl), and a working electrode (mixture of nanocomposite) were used. A mixture of the nanocomposite and a binder (Nafion) were dispersed in absolute ethanol and cast onto the electrode. The potassium hydroxide redox couple was used as the

electrolyte. CV was carried out at scan rates of 5, 25, 50, 75, and 100  $\text{mV s}^{-1}$  in the potential range ( $-1.0$  to  $1.0$  V). The photovoltaic measurements of the fabricated DSSCs with a photoanode active area of  $0.96$   $\text{cm}^2$  were performed with an Oriel Instruments LCS-100 solar simulator accompanied by a Keithley 2420 source meter under one sun illumination (AM 1.5 G,  $100$   $\text{mW cm}^{-2}$ ).

### 3 Results and discussion

The subsequent sections elucidate the physicochemical, electrical conductivity, electrochemical properties, and photovoltaic performance of the nanocomposites.

#### 3.1 Elemental analysis

The incorporation of  $\text{Bi}_2\text{O}_3$  into rGO or heteroatom-doped rGO is evident from the presence of bismuth peaks in the EDX spectrum (Fig. 1). ESI† – Fig. S1(a–f) also shows the EDX elemental mapping of the N-rGO/ $\text{Bi}_2\text{O}_3$  nanocomposite, which confirms that all the constituent elements (carbon, oxygen, nitrogen, and bismuth) were distributed homogeneously in the N-rGO/ $\text{Bi}_2\text{O}_3$  nanocomposite. This was also observed in rGO/ $\text{Bi}_2\text{O}_3$  and B-rGO/ $\text{Bi}_2\text{O}_3$  nanocomposites. The presence of carbon, nitrogen, oxygen, boron, and bismuth in nanocomposites was further confirmed by elemental analysis and ICP-OES (ESI† – Table S1). The  $\text{Bi}_2\text{O}_3$  content in rGO/ $\text{Bi}_2\text{O}_3$ , N-rGO/ $\text{Bi}_2\text{O}_3$ , and B-rGO/ $\text{Bi}_2\text{O}_3$  was found to be 20.8, 28.5, and 25.0%, respectively. N-rGO/ $\text{Bi}_2\text{O}_3$  had a nitrogen content of 3.76%, while B-rGO/ $\text{Bi}_2\text{O}_3$  had a boron content of 2.56%. ATR-

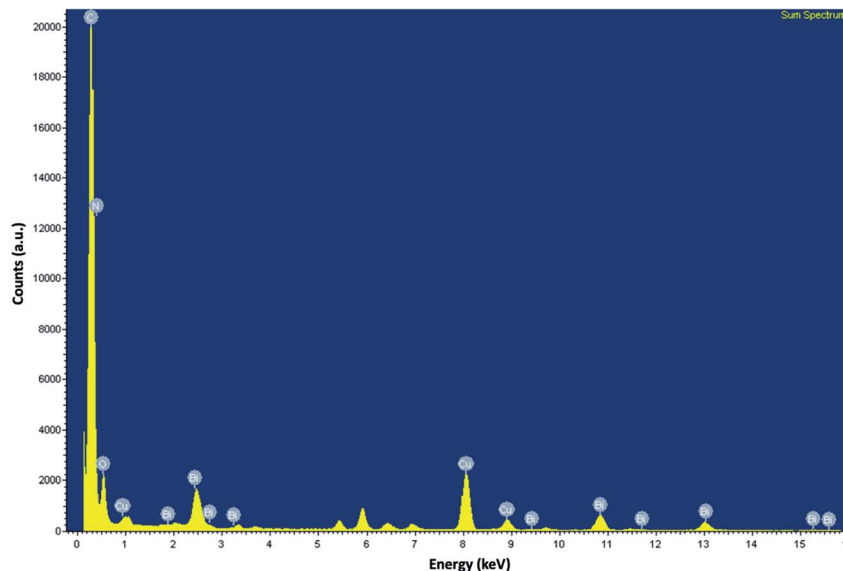


Fig. 1 EDX spectrum of a measurement conducted at the selected area of N-rGO/Bi<sub>2</sub>O<sub>3</sub>.

FTIR was further used to investigate the various functional groups present in the nanocomposites.

### 3.2 Surface functional groups

The ATR-FTIR spectrum of Bi<sub>2</sub>O<sub>3</sub> is shown in Fig. 2 (a), where a peak at 850 cm<sup>-1</sup> is attributed to the symmetrical stretching of Bi–O–Bi, while a peak at 1401 cm<sup>-1</sup> is due to the presence of the metal–oxygen vibration (Bi–O).<sup>40</sup> The heteroatom-doped rGO–Bi<sub>2</sub>O<sub>3</sub>-based nanocomposites exhibited peaks at around 800–850 cm<sup>-1</sup> and 1402 cm<sup>-1</sup>, associated with the Bi–O–Bi and Bi–O vibrations, respectively. The spectra exhibited a broader peak at around 3000–3400 cm<sup>-1</sup> due to the Bi–OH bonds and hydrogen-bonded molecular water species. A weak peak observed at 1665 cm<sup>-1</sup> and 1250 cm<sup>-1</sup> was assigned to N–H bending and C–N stretching in N-rGO/Bi<sub>2</sub>O<sub>3</sub>, respectively. The presence of boron in B-rGO/Bi<sub>2</sub>O<sub>3</sub> was indicated by a peak at around 1180 cm<sup>-1</sup>, which is due to the B–C stretching vibration. Quantitative analysis and ATR-FTIR spectroscopy confirmed the incorporation of Bi<sub>2</sub>O<sub>3</sub> into heteroatom-doped rGO. Thus, to further study the structures of the nanocomposites, TEM and FE-SEM analyses were conducted.

### 3.3 Microstructure and surface morphology

The TEM images in Fig. 3(a)–(c) show wrinkled graphene sheets with Bi<sub>2</sub>O<sub>3</sub> that is uniformly dispersed, indicating the existence of a strong interaction between rGO, N-rGO or B-rGO, and Bi<sub>2</sub>O<sub>3</sub>. Moreover, the interface between Bi<sub>2</sub>O<sub>3</sub> and rGO, N-rGO, or B-rGO shows that the Bi<sub>2</sub>O<sub>3</sub> was well anchored on the sheets. This confirms that Bi<sub>2</sub>O<sub>3</sub> was successfully incorporated into heteroatom-doped rGO as indicated in the EDX spectrum (Fig. 1). Fig. 3(d) and (e) show SEM images, where agglomeration of Bi<sub>2</sub>O<sub>3</sub> is observed in the graphene sheets. N-rGO/Bi<sub>2</sub>O<sub>3</sub> exhibited a high degree of agglomeration due to the high Bi<sub>2</sub>O<sub>3</sub> content.

Consistent with SEM and TEM results, the HRTEM analysis also indicated the successful formation of Bi<sub>2</sub>O<sub>3</sub>-based nanocomposites. Fig. 3(g) to (i) revealed a decrease in interlayer spacing of the Bi<sub>2</sub>O<sub>3</sub>-based nanocomposites compared with rGO, N-rGO, or B-rGO (ESI† – Fig. S2) due to the distortion introduced by the inclusion of Bi<sub>2</sub>O<sub>3</sub> and the reduction of oxygen functional groups, such as carboxyl, epoxy and hydroxyl groups.

### 3.4 Phase composition and defects on the graphitic structure

Fig. 2(b) shows the diffractograms of pure Bi<sub>2</sub>O<sub>3</sub> and the Bi<sub>2</sub>O<sub>3</sub>-based nanocomposites. The P-XRD pattern of pure Bi<sub>2</sub>O<sub>3</sub> shows five intense peaks at 2θ values of 24.7°, 26.8°, 33.5°, 42.0°, and 52.5°, which correspond to the (102), (120), (121), (122), and (321) planes, respectively, confirming the formation of an α phase. These characteristic peaks are confirmed by the reported standard JCPDS file number 76-1730, which is associated with the monoclinic phase with space group *P*2<sub>1</sub>/*c*.<sup>41</sup> When comparing the diffractograms of Bi<sub>2</sub>O<sub>3</sub> and heteroatom-doped rGO–Bi<sub>2</sub>O<sub>3</sub>-based nanocomposites, the diffraction peak representing the carbon species expected at 25° was not observed in all nanocomposites because the diffraction peak was obscured by the stronger diffraction peak of α-Bi<sub>2</sub>O<sub>3</sub>, and due to the low content of rGO, which was below the detection limit.<sup>34,42</sup>

The sharp diffraction peak at 26.8° indicates that Bi<sub>2</sub>O<sub>3</sub> is in a crystalline state, but this peak was reduced after integrating heteroatom-doped rGO with Bi<sub>2</sub>O<sub>3</sub>. Bi<sub>2</sub>O<sub>3</sub> exhibited a relatively high 2θ peak intensity due to the presence of larger nanoparticles with few grain boundaries and low defect density. Theoretically, larger particles have sharp diffraction peaks, while the diffraction peak width increases as the particle sizes are reduced.<sup>43</sup> The most intense diffraction peak (120) was fitted with a Lorentzian distribution function to determine the full-width at half-maximum (FWHM), and the value obtained was



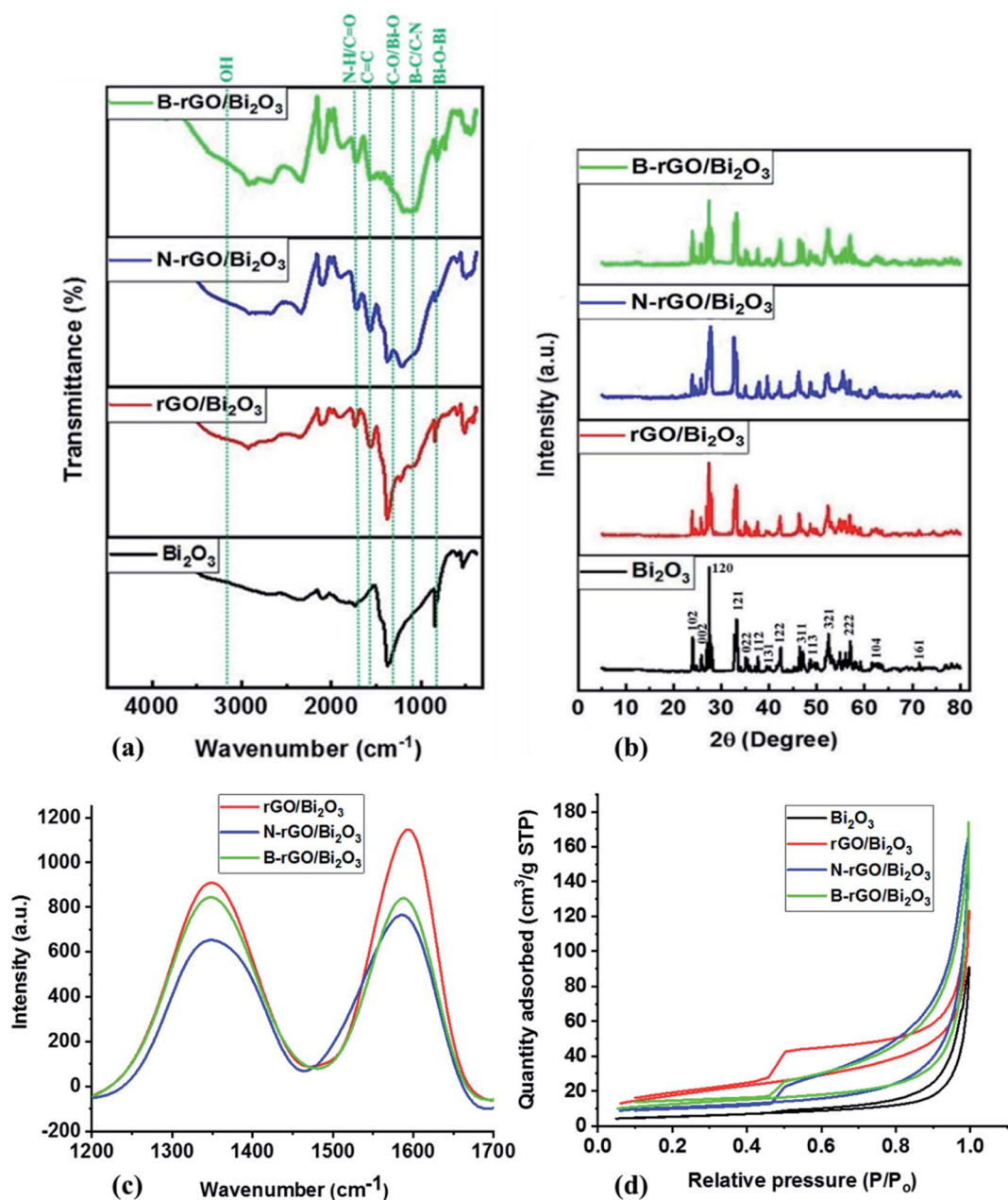


Fig. 2 (a) ATR-FTIR spectra, (b) powder X-ray diffractograms, (c) Raman spectra and (d) N<sub>2</sub> adsorption-desorption isotherms of the Bi<sub>2</sub>O<sub>3</sub>-based nanocomposites.

employed to calculate the crystallite size of the nanocomposites with Scherrer's formula. The crystallite sizes of Bi<sub>2</sub>O<sub>3</sub>, rGO/Bi<sub>2</sub>O<sub>3</sub>, N-rGO/Bi<sub>2</sub>O<sub>3</sub>, and B-rGO/Bi<sub>2</sub>O<sub>3</sub> were 29.2, 20.9, 19.5, and 16.8 nm, respectively. The boron content in B-rGO/Bi<sub>2</sub>O<sub>3</sub> caused an increase in structural strain, thus leading to enhanced surface defects. An interlayer spacing of 0.33 nm was obtained for Bi<sub>2</sub>O<sub>3</sub>, which was comparable to previously reported values.<sup>44,45</sup> The decrease in interlayer spacing after integrating Bi<sub>2</sub>O<sub>3</sub> with heteroatom-doped rGO was caused by lattice distortions, attributed to the incorporation of boron or nitrogen and the decrease in oxygen content during the reduction process.

The crystallite size and graphitic nature of the nanocomposites were further investigated by Raman spectroscopy. The crystallite size ( $L_a$ ) was calculated using eqn (1) reported by Mallet-Ladeira *et al.*<sup>46</sup>

$$\text{WHM} = 71 - 5.2L_a \quad (1)$$

where WHM is the half-width at a half maximum, which is the half of the full width at half maximum (FWHM) when the function is symmetric. The crystallite sizes of Bi<sub>2</sub>O<sub>3</sub>-based nanocomposites were smaller than that of Bi<sub>2</sub>O<sub>3</sub>, indicating that thermal treatment and the type of heteroatom-doping in rGO

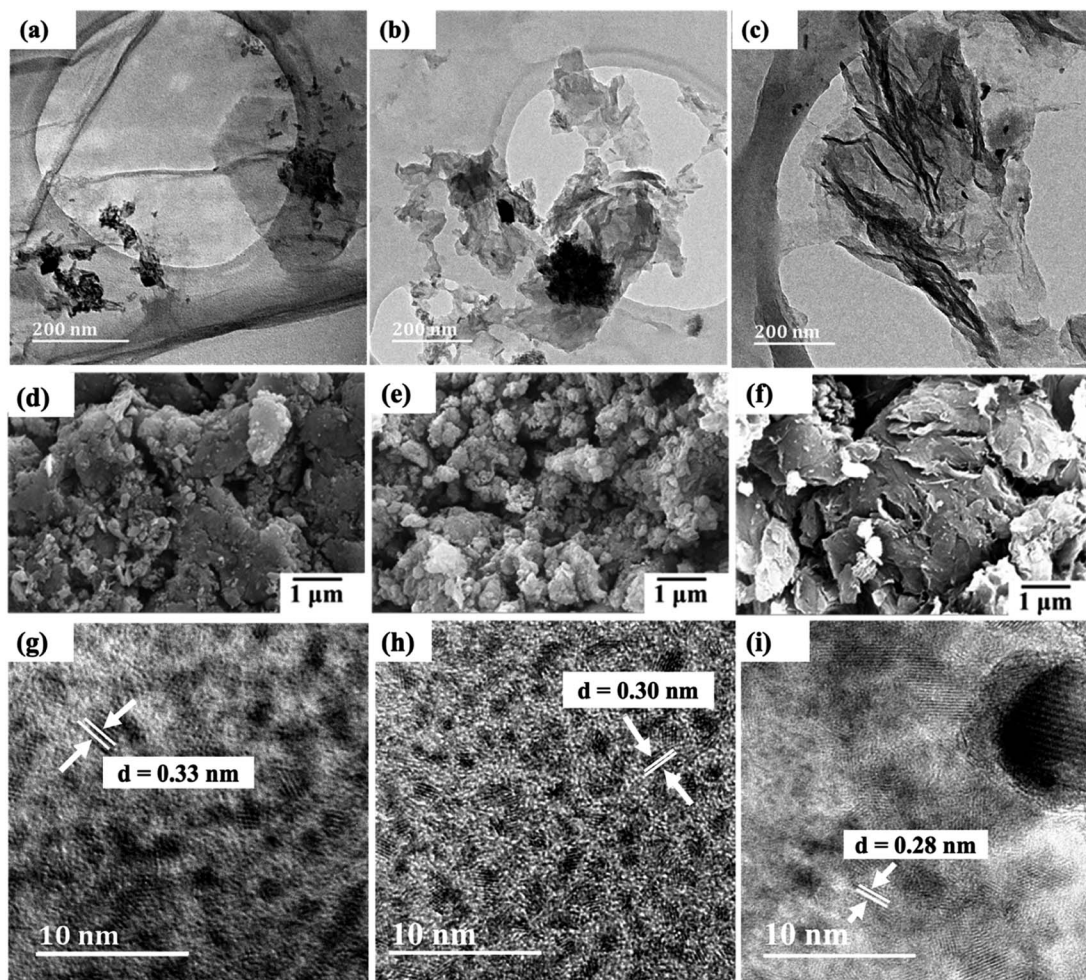


Fig. 3 TEM images of (a) rGO/Bi<sub>2</sub>O<sub>3</sub>, (b) N-rGO/Bi<sub>2</sub>O<sub>3</sub>, and (c) B-rGO/Bi<sub>2</sub>O<sub>3</sub>. SEM images of (d) rGO/Bi<sub>2</sub>O<sub>3</sub>, (e) N-rGO/Bi<sub>2</sub>O<sub>3</sub>, and (f) B-rGO/Bi<sub>2</sub>O<sub>3</sub>. HR-TEM images of (g) rGO/Bi<sub>2</sub>O<sub>3</sub>, (h) N-rGO/Bi<sub>2</sub>O<sub>3</sub>, and (i) B-rGO/Bi<sub>2</sub>O<sub>3</sub>.

affected the crystallite size due to the formation of small crystals. The crystallite sizes from Raman analysis are slightly larger than those from P-XRD analysis; however, they displayed a similar decreasing trend (Table 1).

The graphitic nature of rGO, heteroatom-doped rGO, and Bi<sub>2</sub>O<sub>3</sub>-based nanocomposites was further investigated by Raman spectroscopy. The Raman spectrum of rGO (ESI† – Fig. S3 and Table S2) reveals a D-band at 1350 cm<sup>-1</sup> and a G-band at 1594 cm<sup>-1</sup>, whereby the peak area ratio ( $I_D/I_G$ ) shows

the disorder and the GO structure's graphitic symmetry, respectively. After nitrogen- or boron-doping, the G-bands revealed a minimal shift in the wavenumber. This shift indicated that incorporating nitrogen or boron atoms into the GO lattice prompted an increase in the disordered structure relative to rGO. According to Nanda *et al.*,<sup>47</sup> the shift in the G-band of graphene represents the vibrational mode of sp<sup>2</sup>-hybridized carbon atoms. Thus, the change in the G-band position suggests the change in the number of layers in graphene. The G-band shift towards a higher wavenumber indicates a decrease in the number of graphene layers.

Fig. 2(c) shows that the intensity of the G-band of rGO/Bi<sub>2</sub>O<sub>3</sub> is highest, corresponding to the sp<sup>2</sup> structure of the graphite sheet.<sup>48</sup> The low intensities of the D- and G-band of N-rGO/Bi<sub>2</sub>O<sub>3</sub> suggest a strong interaction between N-rGO and Bi<sub>2</sub>O<sub>3</sub>. This has also been evidenced by the presence of the highest Bi<sub>2</sub>O<sub>3</sub> content in N-rGO/Bi<sub>2</sub>O<sub>3</sub> (ESI† – Table S1) compared with rGO/Bi<sub>2</sub>O<sub>3</sub> and B-rGO/Bi<sub>2</sub>O<sub>3</sub>. Thus, Raman analysis demonstrated the chemical bonding between Bi<sub>2</sub>O<sub>3</sub> and rGO, N-rGO, or B-rGO sheets, in agreement with elemental analysis.

Table 1 P-XRD parameters and crystallinity analysis of the nanocomposites

Sample	P-XRD			Raman	
	2θ/degree	Crystallite size/nm	Interlayer spacing/nm	$I_D/I_G$	Crystallite size/nm
Bi <sub>2</sub> O <sub>3</sub>	26.8	29.2	0.33	—	34.4
rGO/Bi <sub>2</sub> O <sub>3</sub>	27.1	20.9	0.32	1.50	29.6
N-rGO/Bi <sub>2</sub> O <sub>3</sub>	27.9	19.5	0.30	1.79	28.1
B-rGO/Bi <sub>2</sub> O <sub>3</sub>	28.0	16.8	0.30	1.82	27.3

The  $I_D/I_G$  ratio of rGO was lower (0.71 –  $ESI^\dagger$  (Table S2)) due to the reduction of the oxygen functionalities and the recovery of  $sp^2$ -hybridized C–C bonds. However, the  $I_D/I_G$  ratios of N-rGO and B-rGO were higher than for rGO due to structural defects introduced by nitrogen or boron atoms implanted at the radicalized graphene sites. B-rGO displayed an  $I_D/I_G$  ratio of 1.18, which was higher than that of N-rGO (1.09), revealing the presence of a higher degree of disorder in B-rGO than N-rGO.  $Bi_2O_3$ -based nanocomposites showed higher  $I_D/I_G$  ratios than rGO, N-rGO and B-rGO, demonstrating that these nanocomposites possess more defects, with B-rGO/ $Bi_2O_3$  exhibiting the highest  $I_D/I_G$  ratio (1.82).

### 3.5 Surface area and porosity

The specific surface area and pore size of the  $Bi_2O_3$ -based nanocomposites were investigated by the nitrogen adsorption/desorption method (Table 2). The B-rGO/ $Bi_2O_3$  nanocomposite was found to have the largest specific surface area of  $65.5 \text{ m}^2 \text{ g}^{-1}$ . The relatively low surface area of  $53.7 \text{ m}^2 \text{ g}^{-1}$  for rGO/ $Bi_2O_3$  was attributed to the blockage of the rGO lattice by the  $Bi_2O_3$  particles. The larger surface area of nanomaterials is beneficial for enhancing dye loading in the photoanode of DSSCs. Therefore, nanomaterials with a small surface area result in low dye loading, thereby reducing the short-circuit current density ( $J_{sc}$ ) value and the PCE of DSSCs.<sup>49</sup> Thus, to enhance the PCE of DSSCs, the photoanode nanomaterials ought to have a larger surface area. All the nanocomposites exhibited pore sizes below 23 nm, which belong to mesoporous material. Such mesoporous materials with pore sizes between 2 and 50 nm have been widely reported to improve the infiltration of materials in electrolytes.<sup>50,51</sup>

Fig. 2(d) exhibited type IV adsorption–desorption isotherms with an H3 hysteresis loop in the range of 0.45 – 1.0  $P/P_0$ . The H3 hysteresis loop indicates the presence of narrower pores, channel-like pores, and a pore network-linking effect.<sup>52</sup> This again suggests that the synthesised nanocomposites are mesoporous materials. The relative pressure tends to increase ( $P/P_0 > 0.85$ ), and the shape of the adsorption isotherm rises, indicating an increase in the amount of  $N_2$ -adsorption and the presence of capillary condensation in the mesoporous material. This is attributed to the rGO nanomaterial having a larger pore size and being capable of adsorbing a large amount of  $N_2$ .

### 3.6 Thermal stability

The TGA analysis in Fig. 4(a) shows the thermal stability studies represented as TGA thermograms, and  $ESI^\dagger$  (Table S3) shows the decomposition temperatures and residual content of the

nanocomposites. All the nanocomposites exhibited few weight losses around the decomposition temperature of 100 °C, which was attributed to the removal of moisture adsorbed in the interlayers of the nanocomposites. Furthermore, the weight loss that occurred at 200–400 °C is due to the loss of amorphous carbon and other functional groups with the release of  $CO_x$  species. Such decrease in weight in the 200–400 °C range correlates with TEM and SEM analysis (Fig. 3), inferring the presence of amorphous materials. The thermograms indicated that the order of the nanocomposites' tolerance to heat is B-rGO/ $Bi_2O_3$  < N-rGO/ $Bi_2O_3$  < rGO/ $Bi_2O_3$ , *i.e.*, with decomposition temperatures of 437, 490, and 518 °C, respectively. The thermal stability trends agree with the graphitic nature (lower crystallinity) (Raman analysis – Table 1) of the nanocomposites. B-rGO/ $Bi_2O_3$ , with the highest fraction of layered graphene, exhibited the lowest thermal stability of 437 °C and the lowest residual content of  $Bi_2O_3$  of 38%. The highest amount of residue (57%) for N-rGO/ $Bi_2O_3$  could be attributed to some remnant  $Bi_2O_3$  that remains entrapped in the nanocomposite. The elemental analysis also indicates a high  $Bi_2O_3$  content in N-rGO/ $Bi_2O_3$  ( $ESI^\dagger$  – Table S1).

### 3.7 Electrical properties

Four-probe and Hall measurements were used to investigate the electrical conductivity and charge carrier mobility, respectively. Hall effect studies showed that  $Bi_2O_3$ , rGO/ $Bi_2O_3$ , and N-rGO/ $Bi_2O_3$  have n-type charge carriers, while B-rGO/ $Bi_2O_3$  has p-type charge carriers. Such n- and p-type charge carrier characteristics are due to the change in the electronic structure of the nanocomposite. This suggests that N-rGO- $Bi_2O_3$  is a good material for electron transport, while B-rGO/ $Bi_2O_3$  is a good hole transporter. The  $I$ - $V$  characteristics (Fig. 4(b) and Table 3) revealed that the maximum conductivity ( $6.31 \text{ S cm}^{-1}$ ) was obtained from B-rGO/ $Bi_2O_3$  with an improved charge carrier mobility ( $0.368 \text{ cm}^2 \text{ V}^{-1} \text{ s}^{-1}$ ). The improvement in charge carrier mobility is attributed to the decrease in the scattering probability of the charge carriers. The size of boron ions is smaller than that of bismuth ions (the ionic radius of  $B^{3+}$  is 0.23 Å and  $Bi^{3+}$  is 1.17 Å). Thus, there is less scattering of electrons, thereby increasing the charge carrier mobility. B-rGO/ $Bi_2O_3$  had significantly improved electrical conductivity, and this is attributed to its relatively large surface area and high charge carrier mobility.

### 3.8 Electrochemical properties

**3.8.1 Electrode potential characteristics.** The cyclic voltammograms of the samples are shown in Fig. 4(c), where a comparison of  $Bi_2O_3$  and the nanocomposites was obtained at a scanning rate of  $100 \text{ mV s}^{-1}$ . The variation of scan rate, *i.e.*, 5, 25, 50, 75, and  $100 \text{ mV s}^{-1}$  in the  $-1.0$  to  $1.0 \text{ V}$  potential range ( $ESI^\dagger$  – Fig. S4), showed that the cyclic voltammograms maintained certain curve stability,<sup>48,53</sup> indicating that the nanocomposites were mainly electric double layer capacitive.  $Bi_2O_3$  exhibited a small rectangular area, indicating a small capacitance, whereas the  $Bi_2O_3$ -based nanocomposites exhibited extensive background and peak currents. This shows that the effective area of the electrodes was improved, and the electron

Table 2 Textural characterisation of the nanocomposites

Sample	Surface area/ $\text{m}^2 \text{ g}^{-1}$	Pore size/nm
$Bi_2O_3$	4.6	33.52
rGO/ $Bi_2O_3$	53.7	20.37
N-rGO/ $Bi_2O_3$	58.2	22.15
B-rGO/ $Bi_2O_3$	65.5	17.80



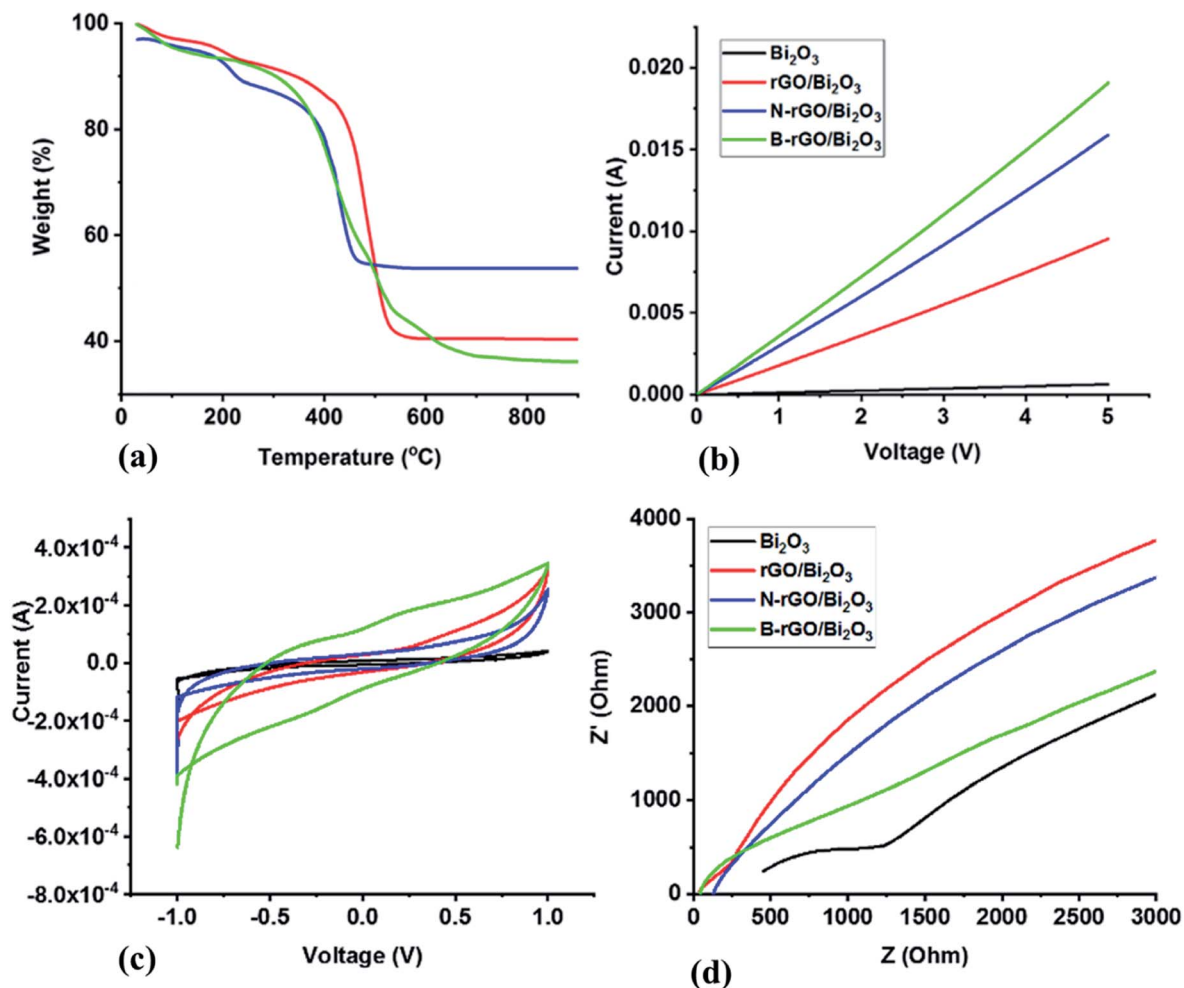


Fig. 4 (a) Thermal stability studies represented as TGA thermograms, (b) current–voltage characteristics, (c) cyclic voltammograms and (d) Nyquist plots of the  $\text{Bi}_2\text{O}_3$ -based nanocomposites.

Table 3 Electrical properties of the  $\text{Bi}_2\text{O}_3$ -based nanocomposites

Sample	Conductivity/ $\text{S cm}^{-1}$	Carrier mobility/ $\text{cm}^2 \text{V}^{-1} \text{s}^{-1}$
$\text{Bi}_2\text{O}_3$	$2.10 \times 10^{-2}$	0.080
rGO/ $\text{Bi}_2\text{O}_3$	3.09	0.267
N-rGO/ $\text{Bi}_2\text{O}_3$	3.84	0.295
B-rGO/ $\text{Bi}_2\text{O}_3$	6.31	0.368

exchange rate was accelerated by the conductive properties of the  $\text{Bi}_2\text{O}_3$ -based nanocomposites.

The presence of oxygen-functional groups in  $\text{Bi}_2\text{O}_3$  decreases its electrical conductivity and deteriorates in the aqueous electrolyte. During the integration of  $\text{Bi}_2\text{O}_3$  with rGO or heteroatom-doped rGO, the oxygen-functional groups were reduced during thermal treatment and the high-pressure environment of the hydrothermal system. Therefore, reducing oxygen-functional groups increased the degree of wetting between the electrode and the electrolyte, thus resulting in an enhanced electrical conductivity, consequently improving the capacitance. A similar observation has been reported by Yang *et al.*,<sup>54</sup> who reported an

increase in the capacitance of highly orientated  $\text{Bi}_2\text{O}_3$ /rGO nanocomposites. The electrochemical activity and electrochemical reversibility are also enhanced due to the introduction of defects and heteroatom-containing groups at the electrode surface, which accelerates the charge transfer rate across the electrode. This also indicates that  $\text{Bi}_2\text{O}_3$ -based nanocomposites have ideal capacitor characteristics. The reversible charge–discharge characteristics in  $\text{Bi}_2\text{O}_3$ -based nanocomposites can probably be attributed to the electrical conductivity of the randomly distributed  $\beta$ - $\text{Bi}_2\text{O}_3$  that is among the  $\alpha$ - and  $\delta$ -phases.<sup>55</sup> Thus, the nanocomposites were further investigated with EIS.

**3.8.2 Interfacial charger transfer characteristics.** For impedance measurements, the  $\text{Bi}_2\text{O}_3$  and  $\text{Bi}_2\text{O}_3$ -based nanocomposite electrodes were characterised *via* Nyquist plots (Fig. 4(d)). The Nyquist plots showed a semicircle corresponding to the faradaic charge transfer resistance ( $R_{ct}$ ) (Table 4) and a linear region, indicating a pure capacitive behaviour and a diffusion-limited process, respectively.<sup>56,57</sup> The  $\text{Bi}_2\text{O}_3$  electrode exhibited a small semicircle in the high-frequency region due to lower resistance. A lower impedance, observed for rGO/ $\text{Bi}_2\text{O}_3$



Table 4 Resistance values for the nanocomposites

Sample	$R_{ct}/\Omega$
$\text{Bi}_2\text{O}_3$	201.1
rGO/ $\text{Bi}_2\text{O}_3$	169.8
N-rGO/ $\text{Bi}_2\text{O}_3$	125.7
B-rGO/ $\text{Bi}_2\text{O}_3$	108.4

compared to  $\text{Bi}_2\text{O}_3$ , led to an improved electron transfer rate. All the heteroatom-doped rGO/ $\text{Bi}_2\text{O}_3$ -based nanocomposites exhibited no semicircle, indicating that the resistance is negligible, thus, suggesting a remarkable charge reversal with a change in voltage. This was attributed to the high electrical conductivity, large specific surface areas, and high nitrogen/boron-doping of the nanocomposites, which provided more sites for enhanced catalytic activity. For instance, in the case of B-rGO/ $\text{Bi}_2\text{O}_3$ , the lack of semicircle was attributed to the largest surface area of B-rGO and its  $\text{sp}^3$  network, which behaves as an electron transport medium from the conduction band of  $\text{Bi}_2\text{O}_3$  to B-rGO. Therefore, the presence of B-rGO in the nanocomposite decreases the charge recombination rate, thus resulting in an enhanced lifetime of the charge carriers.<sup>58</sup>

The series resistance is different for different electrodes used in Fig. 4(d) due to the presence of various oxygen-functional groups in the  $\text{Bi}_2\text{O}_3$ -based nanocomposites. This could also be attributed to the constriction phenomenon of the thick porous film, which had a film thickness of 2  $\mu\text{m}$  that might not be thick enough for electrodes to allow better current collection. Similar observations have been previously reported by Tezyk *et al.*<sup>59</sup>

The  $R_{ct}$  values (Table 4) were calculated from the EIS data. The  $R_{ct}$  values of the  $\text{Bi}_2\text{O}_3$ -based nanocomposites were lower than that of  $\text{Bi}_2\text{O}_3$  due to the free charge transfer in the nanocomposites. The relatively small  $R_{ct}$  values for the nanocomposites indicate that the modification of  $\text{Bi}_2\text{O}_3$  with heteroatom-doped rGO drastically reduces the electrode–electrolyte interfacial resistance. The introduction of heteroatom-doped rGO into  $\text{Bi}_2\text{O}_3$  lowered the  $R_{ct}$  value, which indicates the efficient separation of photogenerated electron–hole pairs and faster interfacial charge transfer. Therefore, heteroatom-doped rGO acts as the conducting channels inside the  $\text{Bi}_2\text{O}_3$  matrix. These results affirm that the effective incorporation of heteroatom-doped rGO sheets improves the electron transport and electrical conductivity of the nanocomposites, resulting in a significant enhancement in electrochemical performance.

### 3.9 Photovoltaic performance of the fabricated DSSCs

DSSCs were fabricated using pure  $\text{Bi}_2\text{O}_3$ , rGO/ $\text{Bi}_2\text{O}_3$ , N-rGO/ $\text{Bi}_2\text{O}_3$ , and B-rGO/ $\text{Bi}_2\text{O}_3$  as photoanodes; and the open-circuit voltage ( $V_{oc}$ ),  $J_{sc}$ , fill factor (FF) and PCE were determined. The photovoltaic properties of DSSCs are listed in Table 5, and the  $J$ – $V$  curves are shown in Fig. 5.  $\text{Bi}_2\text{O}_3$ -based DSSCs exhibited a higher  $V_{oc}$  than rGO/ $\text{Bi}_2\text{O}_3$ -based DSSCs due to back electron transfer (from  $\text{Bi}_2\text{O}_3$  to the redox couple in the electrolyte), which is associated with electrons located in a shallow conduction band edge, thus resulting in a short lifetime. The

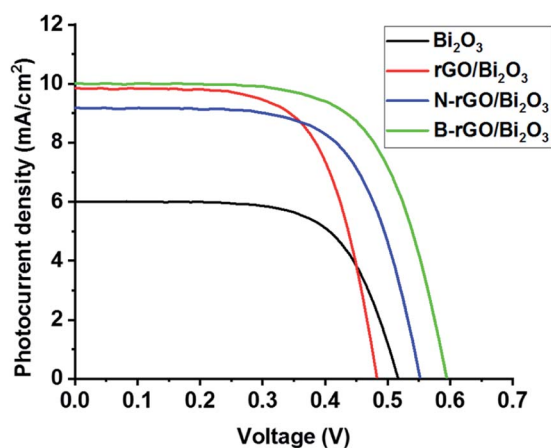
Table 5 Photovoltaic performance of DSSCs with  $\text{Bi}_2\text{O}_3$ -based nanocomposite photoanodes

Photoanode	$V_{oc}/V$	$J_{sc}/\text{mA cm}^{-2}$	FF/%	PCE
$\text{Bi}_2\text{O}_3$	0.53	6.0	20.63	$0.42 \pm 0.04$
rGO/ $\text{Bi}_2\text{O}_3$	0.48	9.8	43.9	$1.68 \pm 0.01$
N-rGO/ $\text{Bi}_2\text{O}_3$	0.55	9.2	47.4	$1.97 \pm 0.02$
B-rGO/ $\text{Bi}_2\text{O}_3$	0.59	10.0	50.2	$2.79 \pm 0.01$

low PCE in the  $\text{Bi}_2\text{O}_3$ -based DSSC is due to poor dye absorption and back recombination at the photoanode–electrolyte interface. A similar observation was reported by Fatima *et al.*,<sup>26</sup> who obtained a PCE of 0.05% for the  $\text{Bi}_2\text{O}_3$ -based DSSC. Poor dye absorption causes a decrease in light absorption, which reduces the photogeneration of charge carriers, and hence, lowers the current density, resulting in poor device performance. Thus, optimisation by surface modification of  $\text{Bi}_2\text{O}_3$  has been used to increase dye absorption and reduce back recombination, thereby improving the performance of DSSCs.

When  $\text{Bi}_2\text{O}_3$ -based nanocomposites were used as a photoanode, the DSSCs exhibited a higher PCE than the  $\text{Bi}_2\text{O}_3$ -based DSSCs. From the EIS analysis and electrical properties of  $\text{Bi}_2\text{O}_3$ -based nanocomposites, it can be suggested that the improvement in PCE is attributed to the low charge transfer resistance and high electrical conductivity of these nanocomposites. When carbon atoms in the graphene lattice are substituted by nitrogen or boron atoms, the conductivity of N-rGO/ $\text{Bi}_2\text{O}_3$  or B-rGO/ $\text{Bi}_2\text{O}_3$  increases remarkably, and the excited electrons are transferred faster in the delocalized  $\pi$  structure of N-rGO/ $\text{Bi}_2\text{O}_3$ -based photoanodes or B-rGO/ $\text{Bi}_2\text{O}_3$ -based photoanodes than rGO/ $\text{Bi}_2\text{O}_3$ -based photoanodes.

B-rGO/ $\text{Bi}_2\text{O}_3$ -based DSSCs exhibited the highest PCE due to enhanced transportation and collection of photogenerated charge carriers. The high PCE is attributed to the hole ( $\text{h}^+$ ) leaving the valence band of B-rGO and quickly moving to the valence band of  $\text{Bi}_2\text{O}_3$ , which facilitates electron and hole ( $\text{e}^-/\text{h}^+$ ) separation. B-rGO has been reported to have a lower bandgap;<sup>60</sup> thus, the lower bandgap of B-rGO is responsible for

Fig. 5  $J$ – $V$  characteristics of the  $\text{Bi}_2\text{O}_3$ -based nanocomposites.

providing a photovoltaic effect in  $\text{Bi}_2\text{O}_3$  with a high bandgap,<sup>61</sup> enhancing charge separation and extending the energy of photoexcitation in DSSCs. Moreover, the electron mobility rate in B-rGO/ $\text{Bi}_2\text{O}_3$  is higher than in rGO/ $\text{Bi}_2\text{O}_3$  and N-rGO/ $\text{Bi}_2\text{O}_3$ , enabling the efficient transportation of electrons and reducing charge recombination. Less charge recombination means more electron density and a shift of the Fermi level, resulting in an increased  $V_{oc}$ . This is consistent with EIS data, in which the B-rGO/ $\text{Bi}_2\text{O}_3$  nanocomposite exhibited the lowest  $R_{ct}$  value. This results in fast electron collection and low charge carrier recombination, leading to the fabrication of a B-rGO/ $\text{Bi}_2\text{O}_3$ -based DSSC with the highest PCE of 2.79%.

The introduction of rGO or heteroatom-doped rGO into  $\text{Bi}_2\text{O}_3$  did not only improve the PCE, but also enhanced the  $J_{sc}$  and  $V_{oc}$  values. In the case of the rGO/ $\text{Bi}_2\text{O}_3$ -based DSSC and N-rGO/ $\text{Bi}_2\text{O}_3$ -based DSSC, low  $V_{oc}$  values of 0.48 and 0.55 V, respectively (Table 5 and Fig. 5), were attributed to faster dye regeneration, which reduces the lifetime of the oxidised dye molecule to suppress charge recombination, thus reducing the  $V_{oc}$ . The presence of a low  $\text{Bi}_2\text{O}_3$  content in rGO/ $\text{Bi}_2\text{O}_3$  increased the  $J_{sc}$  but lowered the  $V_{oc}$ , which substantially reduced the PCE of DSSCs. Although N-rGO/ $\text{Bi}_2\text{O}_3$  showed a higher electrical conductivity and charge carrier mobility than rGO/ $\text{Bi}_2\text{O}_3$ , its performance in DSSCs as a photoanode resulted in a low  $J_{sc}$  due to charge recombination, which is attributed to various bonding configurations of nitrogen (pyrrolic-N, pyridinic-N, and graphitic-N) present on the GO surface.

The  $J_{sc}$  is simultaneously affected by electron transfer efficiency, light scattering, and dye absorption. Thus, the improvement of  $J_{sc}$  is due to the increase in the absorption of dye molecules in DSSCs. The large surface area of the nanocomposite is beneficial for enhancing dye loading in the photoanode of DSSCs. Therefore, the dye molecules are capable of harvesting more light energy for the effective photogeneration of charge carriers. B-rGO/ $\text{Bi}_2\text{O}_3$  had the largest surface area for efficient dye-loading, which increased the  $J_{sc}$  and promoted a higher PCE in DSSCs.

## 4 Conclusion

In summary, heteroatom-doped rGO/ $\text{Bi}_2\text{O}_3$ -based nanocomposites were successfully synthesised and applied as photoanodes in DSSCs. P-XRD analysis showed that pristine  $\text{Bi}_2\text{O}_3$  is in the monoclinic ( $\alpha$ ) form, and this polymorph was maintained even after introducing heteroatom-doped rGO. The heteroatom-doped rGO/ $\text{Bi}_2\text{O}_3$ -based nanocomposites exhibited better catalytic activity than pure  $\text{Bi}_2\text{O}_3$ . Favourable properties, such as large surface area, small pore size, low charge transfer resistance, high charge carrier mobility, and high electrical conductivity, were observed in the heteroatom-doped rGO/ $\text{Bi}_2\text{O}_3$ -based nanocomposites. This demonstrated the suitability of the prepared  $\text{Bi}_2\text{O}_3$ -based nanocomposites as potential photoanode materials for DSSCs. The highest PCE of 2.79% was achieved for the B-rGO/ $\text{Bi}_2\text{O}_3$ -based DSSC, which was attributed to the enhanced channels for electron transfer and electrolyte diffusion. Therefore, the synthesised heteroatom-doped rGO/

$\text{Bi}_2\text{O}_3$ -based nanocomposites are ideal materials for the photoanode in DSSCs.

## Conflicts of interest

There are no conflicts to declare.

## Acknowledgements

The authors would like to thank the National Research Foundation (NRF, Grant numbers – 101357, 116505 and 103979), Moses Kotane Institute, Eskom Tertiary Education Support Programme (TESP), UKZN Nanotechnology Platform, and the University of KwaZulu-Natal for financial support and facilities.

## References

- 1 G. Boschloo, *Front. Chem.*, 2019, 7, 1–9.
- 2 Q. Hualmé, V. M. Mwalukuku, D. Joly, J. Liotier, Y. Kervella, P. Maldivi, S. Narbey, F. Oswald, A. J. Riquelme, J. A. Anta and R. Demadrille, *Nat. Energy*, 2020, 5, 468–477.
- 3 G. George, R. S. Yendaluru and A. Mary Ealias, *Energy Sources, Part A*, 2020, 1, 1–15.
- 4 J. Castro-Gutiérrez, A. Celzard and V. Fierro, *Front. Mater.*, 2020, 7, 1–25.
- 5 Y. Ma, D. Chen, Z. Fang, Y. Zheng, W. Li, S. Xu, X. Lu, G. Shao, Q. Liu and W. Yang, *Proc. Natl. Acad. Sci. U.S.A.*, 2021, 118, e2105610118–e2105610218.
- 6 R. Krishnapriya, C. Nizamudeen, B. Saini, M. S. Mozumder, R. K. Sharma and A. H. I. Mourad, *Sci. Rep.*, 2021, 11, 16265–16277.
- 7 H. Ozawa, Y. Okuyama and H. Arakawa, *Dalton Trans.*, 2012, 41, 5137–5139.
- 8 M. U. Rahman, M. Wei, F. Xie and M. Khan, *Catalysts*, 2019, 9, 273–274.
- 9 P. M. Pataniya, D. Late and C. K. Sumesh, *ACS Appl. Energy Mater.*, 2021, 4, 755–762.
- 10 P. M. Pataniya, V. Patel and C. K. Sumesh, *ACS Appl. Energy Mater.*, 2021, 4, 7891–7899.
- 11 S. Yousaf, S. Zulfiqar, M. I. Din, P. O. Agboola, M. F. Aly Aboud, M. F. Warsi and I. Shakir, *J. Mater. Res. Technol.*, 2021, 12, 999–1009.
- 12 M. Adeel, M. Saeed, I. Khan, M. Muneer and N. Akram, *ACS Omega*, 2021, 6, 1426–1435.
- 13 T. Solaiyammal and P. Murugakoothan, *Mater. Sci. Energy Technol.*, 2019, 2, 171–180.
- 14 R. Chauhan, A. Kumar, G. G. Umarji, U. P. Mulik and D. P. Amalnerkar, *J. Solid State Electrochem.*, 2015, 19, 161–168.
- 15 M. Waghmare, N. Beedri, A. Ubale and H. Pathan, *Eng. Sci.*, 2019, 6, 36–43.
- 16 X. Chen, J. Ye, S. Ouyang, T. Kako, Z. Li and Z. Zou, *ACS Nano*, 2011, 5, 4310–4318.
- 17 A. Birkel, Y.-G. Lee, D. Koll, X. Van Meerbeek, S. Frank, M. J. Choi, Y. S. Kang, K. Char and W. Tremel, *Energy Environ. Sci.*, 2012, 5, 5392–5400.

- 18 K. Yang, R. Li, C. Zhu and J. Pei, *J. Mater. Res.*, 2021, **36**, 2936–2949.
- 19 C. Li, P. He, F. Dong, H. Liu, L. Jia, D. Liu, L. Du, H. Liu, S. Wang and Y. Zhang, *Mater. Lett.*, 2019, **245**, 29–32.
- 20 Y. Qiu, H. Fan, X. Chang, H. Dang, Q. Luo and Z. Cheng, *Appl. Surf. Sci.*, 2018, **434**, 16–20.
- 21 J. M. Bothwell, S. W. Krabbe and R. S. Mohan, *Chem. Soc. Rev.*, 2011, **40**, 4649–4707.
- 22 Y. Qiu, M. Yang, H. Fan, Y. Zuo, Y. Shao, Y. Xu, X. Yang and S. Yang, *CrystEngComm*, 2011, **13**, 1843–1850.
- 23 M. Ciszewski, A. Mianowski, P. Szatkowski, G. Nawrat and J. Adamek, *Ionics*, 2015, **21**, 557–563.
- 24 M. Schlesinger, S. Schulze, M. Hietschold and M. Mehring, *Dalton Trans.*, 2013, **42**, 1047–1056.
- 25 S. Shaikh, G. Rahman, R. S. Mane and O.-S. Joo, *Electrochim. Acta*, 2013, **111**, 593–600.
- 26 M. J. Jabeen Fatima, C. V. Niveditha and S. Sindhu, *RSC Adv.*, 2015, **5**, 78299–78305.
- 27 P. Fernández-Ibáñez, M. I. Polo-López, S. Malato, S. Wadhwa, J. W. J. Hamilton, P. S. M. Dunlop, R. D'Sa, E. Magee, K. O'Shea, D. D. Dionysiou and J. A. Byrne, *Chem. Eng. J.*, 2015, **261**, 36–44.
- 28 E. Kusiak-Nejman, A. Wanag, Ł. Kowalczyk, J. Kapica-Kozar, C. Colbeau-Justin, M. G. Mendez Medrano and A. W. Morawski, *Catal. Today*, 2017, **287**, 189–195.
- 29 J. P. Mensing, C. Poochai, S. Kerdpocha, C. Sriprachuabwong, A. Wisitsoraat and A. Tuantranont, *Adv. Nat. Sci.: Nanosci. Nanotechnol.*, 2017, **8**, 033001–033008.
- 30 M. I. A. Abdel Maksoud, R. A. Fahim, A. E. Shalan, M. Abd Elkodous, S. O. Olojede, A. I. Osman, C. Farrell, A. H. Al-Muhtaseb, A. S. Awed, A. H. Ashour and D. W. Rooney, *Environ. Chem. Lett.*, 2021, **19**, 375–439.
- 31 C. K. Chua and M. Pumera, *Chem. Soc. Rev.*, 2014, **43**, 291–312.
- 32 Z. Bo, Z. Wen, H. Kim, G. Lu, K. Yu and J. Chen, *Carbon*, 2012, **50**, 4379–4387.
- 33 F. M. Ascencio Aguirre and R. Herrera Becerra, *Appl. Phys. A*, 2015, **119**, 909–915.
- 34 X. Liu, L. Pan, T. Lv, Z. Sun and C. Q. Sun, *J. Colloid Interface Sci.*, 2013, **408**, 145–150.
- 35 T. Kuila, S. Bose, A. K. Mishra, P. Khanra, N. H. Kim and J. H. Lee, *Prog. Mater. Sci.*, 2012, **57**, 1061–1105.
- 36 D.-Y. Yeom, W. Jeon, N. D. K. Tu, S. Y. Yeo, S.-S. Lee, B. J. Sung, H. Chang, J. A. Lim and H. Kim, *Sci. Rep.*, 2015, **5**, 9817–9836.
- 37 S. Pei and H.-M. Cheng, *Carbon*, 2012, **50**, 3210–3228.
- 38 N. P. D. Ngidi, M. A. Ollengo and V. O. Nyamori, *Materials*, 2019, **12**, 3376–3401.
- 39 N. P. D. Ngidi, M. A. Ollengo and V. O. Nyamori, *New J. Chem.*, 2020, **44**, 16864–16876.
- 40 Y. Astuti, B. M. Listyani, L. Suyati and A. Darmawan, *Indones. J. Chem.*, 2021, **21**, 108–117.
- 41 M. Malligavathy and D. P. Padiyan, *Adv. Mater. Processes*, 2017, **2**, 51–55.
- 42 H. Zhang, X. Lv, Y. Li, Y. Wang and J. Li, *ACS Nano*, 2010, **4**, 380–386.
- 43 Z. A. Zulkifli, K. A. Razak and W. N. W. A. Rahman, *AIP Conf. Proc.*, 2017, **1901**, 020011–020016.
- 44 M. Jalalah, M. Faisal, H. Bouzid, J.-G. Park, S. A. Al-Sayari and A. A. Ismail, *J. Ind. Eng. Chem.*, 2015, **30**, 183–189.
- 45 E. Pargoletti, S. Mostoni, G. Rasso, V. Pifferi, D. Meroni, L. Falciola, E. Davoli, M. Marelli and G. Cappelletti, *Environ. Sci. Pollut. Res.*, 2017, **24**, 8287–8296.
- 46 P. Mallet-Ladeira, P. Puech, C. Toulouse, M. Cazayous, N. Ratel-Ramond, P. Weisbecker, G. L. Vignoles and M. Monthieux, *Carbon*, 2014, **80**, 629–639.
- 47 S. S. Nanda, M. J. Kim, K. S. Yeom, S. S. A. An, H. Ju and D. K. Yi, *TrAC, Trends Anal. Chem.*, 2016, **80**, 125–131.
- 48 W.-D. Yang and L. Yu-Jiang, *J. Electr. Eng.*, 2019, **70**, 101–106.
- 49 K. Song, I. Jang, D. Song, Y. S. Kang and S.-G. Oh, *Sol. Energy*, 2014, **105**, 218–224.
- 50 G. Gryglewicz, J. Machnikowski, E. Lorenc-Grabowska, G. Lota and E. Frackowiak, *Electrochim. Acta*, 2005, **50**, 1197–1206.
- 51 S. Liu, Y. Wang and Z. Ma, *Int. J. Electrochem. Sci.*, 2018, **13**, 12256–12265.
- 52 K. S. Sing and R. T. Williams, *Adsorp. Sci. Technol.*, 2004, **22**, 773–782.
- 53 H. Shen, Y. Zhang, X. Song, Y. Liu, H. Wang, H. Duan and X. Kong, *J. Alloys Compd.*, 2019, **770**, 926–933.
- 54 W.-D. Yang and Y.-J. Lin, *Int. J. Electrochem. Sci.*, 2020, **15**, 1915–1929.
- 55 X. Yang, X. Lian, S. Liu, G. Wang, C. Jiang, J. Tian, J. Chen and R. Wang, *J. Phys. D: Appl. Phys.*, 2012, **46**, 035103–035110.
- 56 T. Zhan, X. Wang, X. Li, Y. Song and W. Hou, *Sens. Actuators, B*, 2016, **228**, 101–108.
- 57 Z. Wei, Y. Wang and J. Zhang, *Sci. Rep.*, 2018, **8**, 6929–6937.
- 58 X. Bai, X. Zhang, Z. Hua, W. Ma, Z. Dai, X. Huang and H. Gu, *J. Alloys Compd.*, 2014, **599**, 10–18.
- 59 V. Tezyk, C. Rossignol, N. Sergent, E. Djurado, J. Laurencin and E. Siebert, *Electrochim. Acta*, 2019, **304**, 312–322.
- 60 M. Junaid, M. H. M. Khir, G. Witjaksono, N. Tansu, M. S. M. Saheed, P. Kumar, Z. Ullah, A. Yar and F. Usman, *Molecules*, 2020, **25**, 3646–3665.
- 61 J. Li, B. Z. Wu and Z. X. Zhou, *Micro Nano Lett.*, 2018, **13**, 1443–1446.